

Article

REE Minerals as Geochemical Proxies of Late-Tertiary Alkalic Silicate ± Carbonatite Intrusions Beneath Carpathian Back-Arc Basin

Vratislav Hurai ^{1,*}, Monika Huraiová ² and Patrik Konečný ³¹ Earth Science Institute, Slovak Academy of Sciences, 840 05 Bratislava, Slovakia² Department of Mineralogy and Petrology, Comenius University, 842 15 Bratislava, Slovakia; monika.huraiova@uniba.sk³ State Geological Institute of Dionýz Štúr, 817 04 Bratislava, Slovakia; patrik.konecny@geology.sk

* Correspondence: vratislav.hurai@savba.sk

Abstract: The accessory mineral assemblage (AMA) of igneous cumulate xenoliths in volcanoclastic deposits and lava flows in the Carpathian back-arc basin testifies to the composition of intrusive complexes sampled by Upper Miocene-Pliocene basalt volcanoes. The magmatic reservoir beneath Pinciná maar is composed of gabbro, moderately alkalic to alkali-calcic syenite, and calcic orthopyroxene granite (pincinite). The intrusive complex beneath the wider area around Fil'akovo and Hajnáčka maars contains mafic cumulates, alkalic syenite, carbonatite, and calc-alkalic granite. Both reservoirs originated during the basaltic magma underplating, differentiation, and interaction with the surrounding mantle and crust. The AMA of syenites is characterized by yttrialite-Y, britholite-Y, britholite-Ce, chevkinite-Ce, monazite-Ce, and rhabdophane(?). Baddeleyite and REE-zirconolite are typical of alkalic syenite associated with carbonatite. Pyrochlore, columbite-Mn, and Ca-niobates occur in calc-alkalic granites with strong peralkalic affinity. Nb-rutile, niobian ilmenite, and fergusonite-Y are crystallized from mildly alkalic syenite and calc-alkalic granite. Zircon with increased Hf/Zr and Th/U ratios occur in all felsic-to-intermediate rock-types. If rock fragments are absent in the volcanic ejecta, the composition of the sub-volcanic reservoir can be reconstructed from the specific AMA and zircon xenocrysts–xenolith relics disintegrated during the basaltic magma fragmentation and explosion.

Keywords: yttrialite; britholite; zirconolite; chevkinite; syenite; carbonatite; basalt; Western Carpathians



Citation: Hurai, V.; Huraiová, M.; Konečný, P. REE Minerals as Geochemical Proxies of Late-Tertiary Alkalic Silicate ± Carbonatite Intrusions Beneath Carpathian Back-Arc Basin. *Minerals* **2021**, *11*, 369. <https://doi.org/10.3390/min11040369>

Academic Editors: Ján Spišiak, Jaroslav Pršek, Jiří Sejkora and Nigel J. Cook

Received: 27 January 2021

Accepted: 27 March 2021

Published: 31 March 2021

Publisher's Note: MDPI stays neutral with regard to jurisdictional claims in published maps and institutional affiliations.



Copyright: © 2021 by the authors. Licensee MDPI, Basel, Switzerland. This article is an open access article distributed under the terms and conditions of the Creative Commons Attribution (CC BY) license (<https://creativecommons.org/licenses/by/4.0/>).

1. Introduction

Direct information about the composition of the deep lithosphere is encoded in rock fragments (xenoliths) ejected by basaltic volcanoes. The vast majority of smaller rock fragments scavenged from the walls of volcanic conduits is resorbed in the hot basalt, whereas the larger xenoliths are disintegrated and ground during the magma fragmentation and phreatomagmatic eruption triggered by the magma-water interaction and explosive release of rapidly expanding gas bubbles. Consequently, only specific accessory mineral assemblage (AMA) is preserved, consisting of phenocrysts crystallized from the magma and xenocrysts derived from the disintegrated xenoliths. Detailed knowledge of morphology, composition, zoning, and elemental substitutions in individual accessory minerals is necessary to decipher the information on the composition of rocks sampled by the ascending magma [1,2].

Upper Miocene–Quaternary basaltic pyroclastic deposits in the northern part of the Pannonian Basin (Carpathian back-arc basin) contain a unique assemblage of igneous xenoliths [3], and significantly more abundant spinel peridotite and wehrlite xenoliths transported from the metasomatized upper mantle [4]. Gabbroic and syenite xenoliths represent gravitational and flotation cumulates, respectively, scavenged from stratified, partly

solidified magmatic intrusions [5]. Occasional granite fragments range in composition from barren magnesian and calcic orthopyroxene granite (pincinite) to productive, HFSE- and REE-rich ferroan calc-alkalic granite [6–8]. Despite the diverse compositions, trace elements and radiogenic isotopes define the whole suite of igneous xenoliths as a cogenetic assemblage of an Upper Miocene–Pliocene A₁-type intra-plate continental magmatism [9].

Here we investigate the AMA of igneous xenoliths and tuff from one classical (Pinciná maar) and one newly discovered (Hajnáčka diatrema) locality. We compare the AMAs of various syenite types with productive calc-alkaline granites. We furthermore demonstrate that the composition of sub-volcanic magmatic intrusive complexes can be inferred from the specific AMA recovered from pyroclastic deposits. The information obtained from AMA can be supplemented by the chemical composition of crystal-melt inclusions enclosed in zircon xenocrysts, which represent refractory relics of igneous xenoliths disintegrated during explosion.

2. Geological Setting

The volcanoes studied belong to the Late Miocene–Late Pleistocene alkali basalt province of the Pannonian Basin (Figure 1), which is an intra-Carpathian back-arc basin characterized in the northern part by a moderate crustal thickness (26–28 km) and a 70–90 km thick lithospheric mantle [10,11]. Spatially isolated monogenetic volcanoes of the alkali basalt province originated from the post-rift thermal subsidence superimposed on Middle Miocene, Alpine-type, gravity-driven subduction coincidental with the collision of the ALCAPA (ALpine-CARpathian-PANnonian) and Tisza-Dacia microplates with the European plate [12]. The Miocene subduction was compensated by the diapiric rise of the asthenosphere and the decompression melting of the lithospheric mantle [12,13], giving rise to basanite, basalt-trachybasalt, and tephrite-phonotephrite magmas erupted in the time interval between 8 and 0.2 Ma [14,15].

The Pinciná maar (48°21′52.47″ N, 19°46′17.04″ E, Figure 2), 760 × 930 m in area, was created by phreatomagmatic eruptions in the fluvial-lacustrine environment of the Pontian Poltár formation of the Lučenec Basin—the northernmost promontory of the Pannonian Basin. The burial beneath the sediments preserved the Pinciná maar from erosion and destruction [16]. The southern part of the maar is overlain by marine littoral and shallow shelf sediments of the Egerian Szécsény Schlier. According to indirect geological evidence [17], the Pinciná maar was affiliated with the earliest Late Pannonian (~7–8 Ma) volcanic pulse. However, U-Pb-Th and (U-Th)/He geochronology applied to zircon, monazite, and apatite fragments isolated from volcanoclastic material and igneous xenoliths yielded considerably younger ages, 5.2–5.4 Ma, overlapping the Upper Miocene–Pliocene boundary [1,18]. Syenite xenoliths and detrital zircons with REE minerals mentioned in this study have been extracted from friable tuff deposits exposed in the south-western wall of the maar structure.

The Hajnáčka diatrema (48°13′5.25″ N, 19°57′18.59″ E, Figure 2) in the Cerová Upland is a feeder conduit of a basaltic maar, towering about 75 m above the surrounding Quaternary river terrace. The diatrema has been assigned to the early Romanian third volcanic phase [15], according to a 2.7 ± 0.5 Ma K–Ar whole-rock age of intersecting basalt dike [16]. The (U-Th-Sm)/He dating of apatite recovered from the block of friable basaltic tuff yielded an age of 2.1 ± 0.2 Ma [1]. The carbonatite syenite xenolith studied, about 2 × 3 cm in size, was isolated from the welded tuffaceous breccia exposed atop the diatrema.

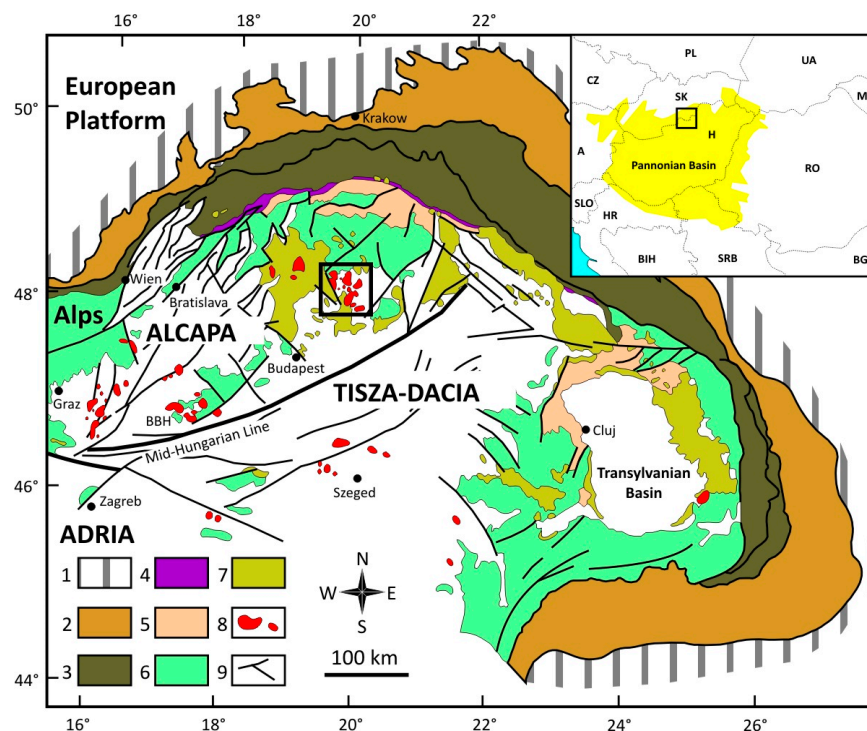


Figure 1. Schematic drawing of the Carpathian arc and the intra-Carpathian back-arc basin (Pannonian Basin) modified after [19]. Explanations: 1. European (W) and Skythian (E) platforms; 2. foredeep, 3. Tertiary accretionary wedge, 4. Klippen belt, 5. Palaeogene back-arc basin, 6. Variscan basement with pre-Tertiary sedimentary cover and Mesozoic nappe units (Cretaceous accretionary wedge), 7. Neogene andesites and rhyolites, 8. Upper Miocene–Quaternary alkali basalt, 9. Major normal, strike-slip, and thrust faults. Inset shows state boundaries. Rectangle marks the south-Slovakian volcanic province enlarged in Figure 2.

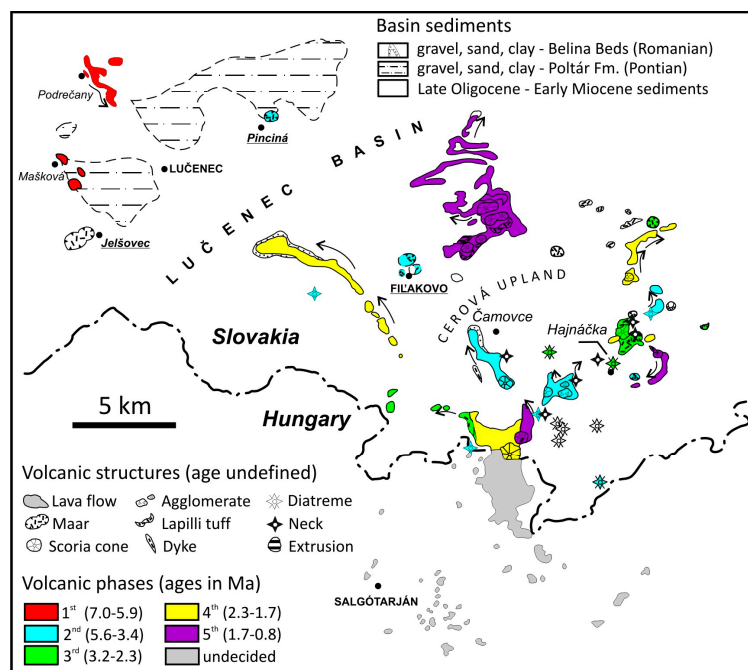


Figure 2. Enlarged view of the study area with volcanic phases inferred from geochronology [1,14–16,18–20].

3. Methods

Chemical compositions of minerals and silicate glass were determined using a wavelength-dispersive (WDS) mode of CAMECA SX-100 electron probe micro-analyzer maintained in the State Geological Survey of Dionýz Štúr, Bratislava, Slovakia. An accelerating voltage of 15 kV was used to optimize the spatial resolution and matrix correction factors, and minimize the sample surface damage. Beam diameters ranged between 2 μm and 5 μm for minerals and 20 μm for silicate glass (if possible). Excitation lines, crystals, calibrants, average detection limits, and average standard deviations are summarized in the Table S1. Matrix effects were resolved using the X-PHI correction method [21]. Spectral lines unaffected by interferences were selected. When peak overlaps existed, empirical correction factors [22,23] were applied.

4. Results

4.1. Petrography and Mineralogy

Syenite xenoliths in the pyroclastic deposits of Pinciná maar are either encapsulated in basalt bombs or occur as angular fragments and blocks up to 30 cm in size in friable lapilli tuffs. The syenites are almost monomineral feldspar-rich rocks devoid of mafic minerals, showing an equi-granular texture composed of feldspar interlocked with less than 10 vol.% of opaque brown to translucent yellow intergranular glass. The investigated samples, PI-12 and HP-3, belong to the group of less-oxidized syenite xenoliths, having $16 \pm 1\%$ Fe^{3+} relative to total iron in the silicate glass [5]. Whole-rock chemical analyses of the xenoliths are listed in the Table S2.

The feldspar composition spans the interval from Na-sanidine, through anorthoclase, to albite. The silicic intergranular glass is quartz-normative peraluminous, occasionally metaluminous, trachyte to alkalic rhyolite. The opaque brown domains in the glass are enriched in FeO_{tot} relative to the translucent parts by 2–3 wt.% and often contain an immiscible Fe-oxide phase [5].

Dark red to pink zircons, up to 1 mm in size, occur in the intergranular glass. All zircons exhibit simple combinations of prismatic (100) > (110) and pyramidal (101) forms characteristic of high-temperature alkaline series granites. Zircon fragments recovered from the friable white tuff (sample P-4) have the same typomorphic characteristics and represent refractory relics of smaller syenite xenoliths disintegrated during phreatomagmatic eruption.

REE-bearing silicates and phosphates occur as daughter phases of silicate melt inclusions in zircons and crystal aggregates in feldspar-silicate melt matrix intimately intergrown or replaced by a hydrous Ce-phosphate (Figure 3). Apart from zircon, the AMA of syenites from Pinciná maar also involves Mg-magnetite, corundum, apatite, titanite, monazite-Ce (Table S3), uranothorianite, uranothorite, and fergusonite (Table S4). The silicate glass enclosed in inclusions corresponds to potassic trachyte (Table S5).

Syenite xenolith HA-8 recovered from the Hajnáčka diatreme is composed of K-feldspar, quartz, and interstitial silicate-carbonate glass. The xenolith texture is reminiscent of a hydraulic breccia with chaotically distributed, partially melted quartz, and feldspar grains cemented by the silicate glass and amoeboid Mg-calcite ocelli (Figure 4). The feldspar compositions span the range from anorthoclase to Na-sanidine, the latter occurring along rims and contacts with the silicate-carbonate glass matrix. Rare mafic minerals are represented by the aluminian-ferroan aegirine-augite replaced by ferrian hedenbergite (Figure 4a).

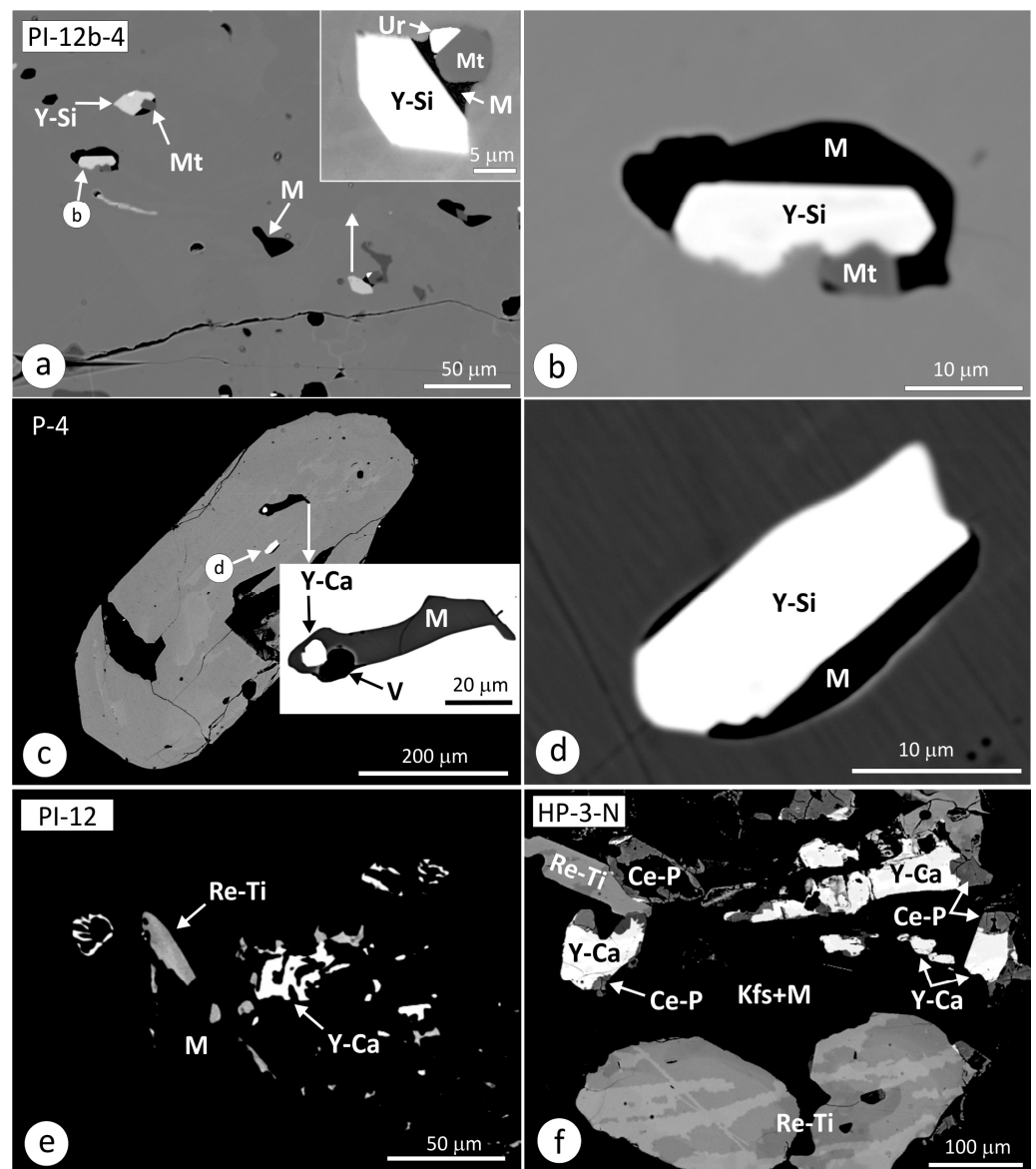


Figure 3. Back-scattered electron (BSE) images of yttrium silicates and associated minerals in syenite xenoliths and volcanic tuff ejected in the Pinciná maar. (a) Part of a large zircon crystal, 1 mm in size, in syenite xenolith showing numerous inclusions of silicate glass (M) and crystal aggregates composed of yttrium silicate (Y-Si), magnetite (Mt), and uranothorianite (Ur). Inset shows close-up of one of the crystal–glass aggregates. (b) Magnified view of the inclusion from the previous image, showing euhedral yttrium silicate, magnetite, and silicate glass. (c,d) Zircon isolated from volcanic tuff with two bright yttrium silicate crystals embedded in silicate glass (M). The close-up documents an elongated silicate glass inclusion with vapour bubble (V) and bright Ca-Y silicate (Y-Ca). Another yttrium silicate (Y-Si) embedded in silicate melt is documented in (d). (e,f) BSE images documenting the close spatial relationship of REE-Ti silicate (Re-Ti), Y-Ca silicate (Y-Ca), and Ca-Ce phosphate (Ca-Ce) in syenite xenolith HP-3. Dark matrix is composed of potassium feldspar (Kfs) and silicate glass (M).

The silicate glass domains that appear dark in BSE contrast represent molten feldspars, as is documented by the almost identical chemical compositions of both, and negligible amounts of Fe, Ti, Mg-oxides. Brighter domains with increased Fe, Ti, and Mg and lower Si contents correspond to potassic trachyte (Table S5).

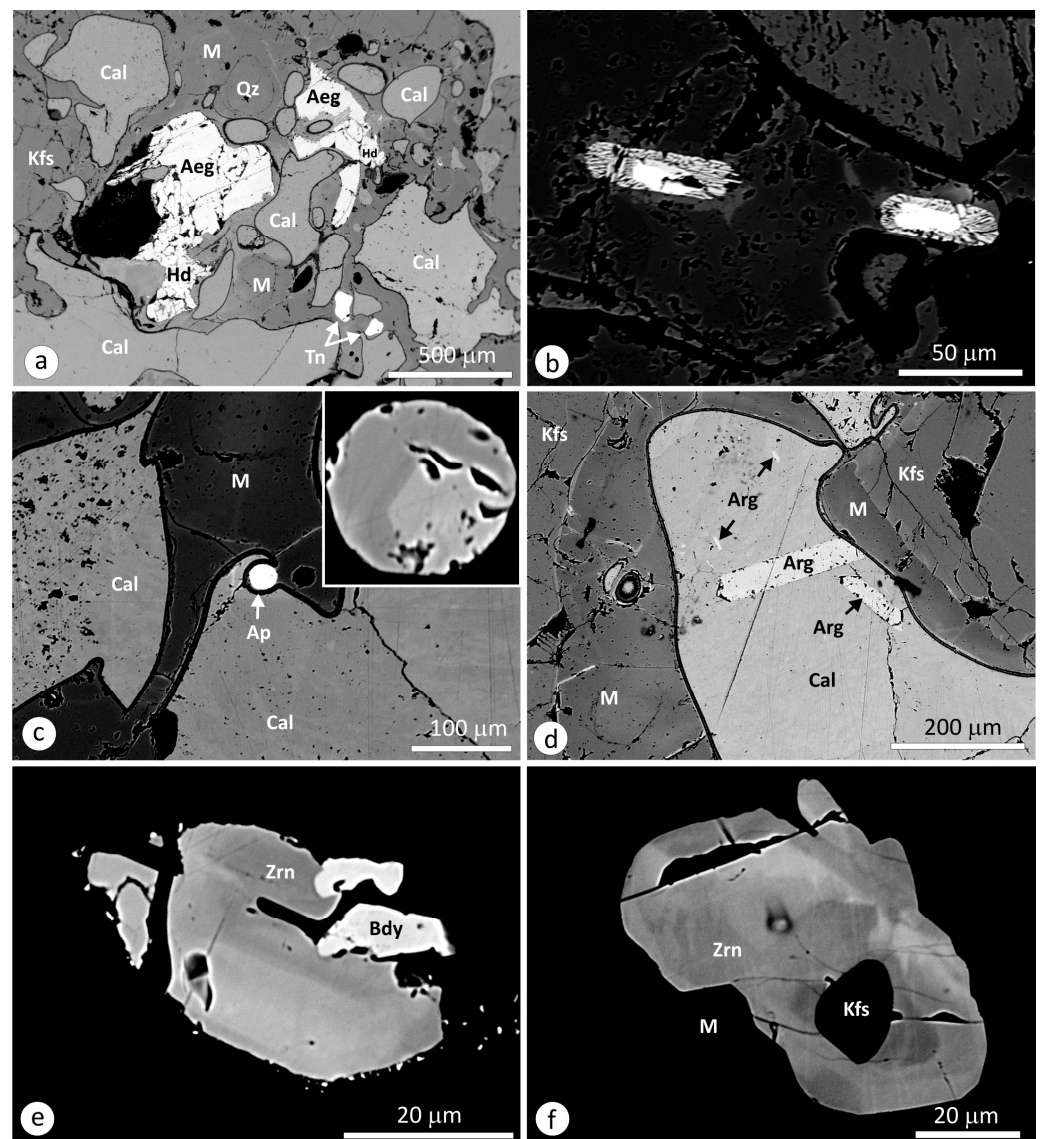


Figure 4. Back-scattered electron images of accessory minerals in carbonatite-syenite xenolith HA-8 from Hajnáčka diatreme. (a) Microscopic view documenting rounded calcite blebs embedded in a silicate glass matrix and partly resorbed grains of titanite and aegirine replaced by hedenbergite. (b) Coronal rutile replacing resorbed ilmenite crystals. (c) Apatite globule embedded within silicate glass, partly encompassed by carbonate. Enlarged view in the inset documents a growth zoning of the resorbed crystal. Deformation of calcite around the globular apatite testifies to the carbonate liquid. (d) Aragonite crystals grown from the interface between silicate and carbonate phases. One of the two larger aragonites was detached from the original position during the carbonate liquid movement. Perfect euhedral shapes indicate the equilibrium crystallization from the carbonatite liquid. (e) Zirconolite–baddeleyite aggregate in the interstitial glass matrix. (f) Domain-zoned zirconolite embedded in silicate glass. Brighter domains are enriched in Th and REE, whereas less bright domains are enriched in Ti and Ca. Abbreviations: Aeg—*aegirine-augite*, Ap—*apatite*, Arg—*aragonite*, Bdy—*baddeleyite*, Cal—*calcite*, Hed—*hedenbergite*, Kfs—*eldspar*, M—*silicate glass*, Tn—*titanite*, Qz—*quartz*, Zrn—*zirconolite*.

The carbonate ocelli show polygonal fibrous texture in transmitted light, and fine domain zoning in back-scattered electron images (Figure 4a,c,d). Some ocelli contain aragonite crystals growing from the silicate glass-carbonate and feldspar-carbonate boundaries. Small aragonite crystals appear freely suspended in the ocelli without any preferred orientation (Figure 4d). X-ray and Raman mapping [24] revealed an incremental oscillatory

growth zoning of aragonite, contrasting with an irregular patchy domain microtexture of the associated Mg-calcite.

The AMA of syenite xenolith HA-8 consists of ilmenite, rutile, titanite, barite, baddeleyite, zircon, apatite, and zirconolite. Manganous to magnesian ilmenite with 1–2 wt.% Nb₂O₅ is replaced along grain boundaries by Nb-rutile symplectite (Figure 4b) with 2.3–7.3 wt.% Nb₂O₅ (Table S6).

Euhedral fluorapatite is enclosed in feldspars. Resorbed apatites occur in the interstitial silicate glass. Both morphological types exhibit growth zoning with the brighter core enriched in REE and darker margins depleted in REE (Figure 4c, Table S7).

Titanite creates rounded resorbed grains in the silicate-carbonate glass matrix. BSE images revealed complex titanite zoning. Nb-poor cores with primary magmatic oscillatory zoning are replaced from grain boundaries by at least four metasomatic zones with gradually increasing (Nb,Ta)₂O₅ and ZrO₂ contents, reaching the maximum concentrations of up to 6.9 and 1.0 wt.%, respectively, in the marginal zone. The total YREE oxide content attains 4.5 wt. % (Table S8).

Zirconolite (Figure 4e,f) forms irregular opaque grains with brown translucent margins enclosed in the interstitial glass or rock-forming feldspar. Some zirconolite grains are intergrown with baddeleyite (Figure 4e,f), which contains 1.3–2.3 wt.% Nb₂O₅ + Ta₂O₅ and 1.4–1.8 wt.% HfO₂ (Table S9). The zirconolites enclosed in feldspars are closely spatially associated with zircon with an HfO₂ content up to 1.6 wt.% (Table S9).

4.2. Substitutions in REE-Bearing Silicates and Phosphates

4.2.1. Chevkinite

Electron probe micro-analyses of REE-Ti-silicates from Pinciná (Table S10) recalculated on the basis of 22 (O,F,Cl) correspond to an almost ideal chevkinite formula (REE,Ca,Th)₄Fe²⁺(Fe³⁺,Fe²⁺,Ti,Al,Mn)₂Ti₂Si₄O₂₂, with perfect substitution in the crystallographic sites A and C according to the scheme: (Ca + Sr)_A + (Ti + Zr)_C = (Y + REE)_A + (M³⁺ + M²⁺)_C, where M³⁺ and M²⁺ refer to tri- and divalent cations, respectively [25] (Figure 5). The total sum of cations is greater than 13, thus indicating the presence of ferric iron, with calculated concentrations between 0.3 and 1 apfu, along with ferrous iron. Lower analytical totals testify to the presence of either OH or metamictization. However, FeO and CaO variations coincide with those in primary magmatic, non-altered chevkinite-Ce (Figure 6a), and the same is indicated by the negatively correlated Ti_C and Th contents (Figure 6b).

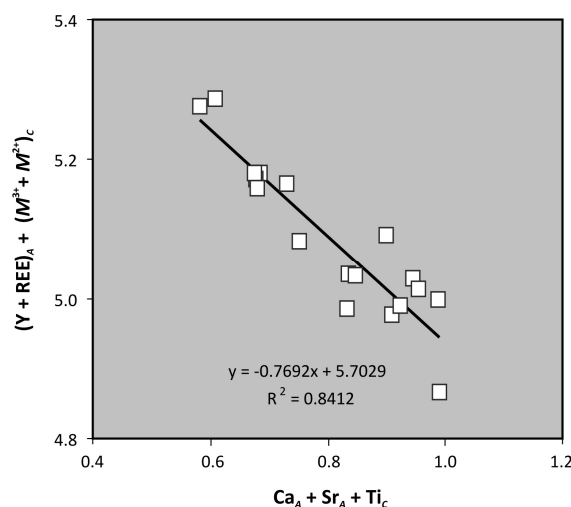


Figure 5. Correlation between A- and C-site cations (apfu) in chevkinite-Ce from Pinciná.

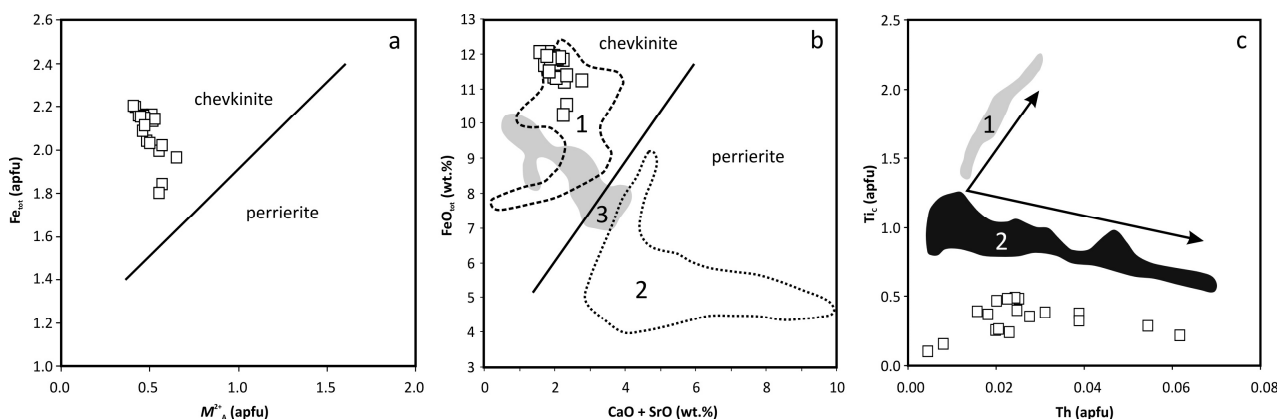


Figure 6. (a,b) Chevkinite-perrierite discrimination diagrams [26,27] with fields for non-altered chevkinite (1), perrierite (2), and hydrothermally altered chevkinite and perrierite (3) from A-type syenites and granites of Brasil [28]. (c) Correlation between titanium and thorium contents (apfu), illustrating compositional trends in post-magmatic (2) and primary magmatic (1) chevkinite [28]. Squares are projection points of chevkinites from Pinciná.

4.2.2. Yttrialite–britholite-Y

Two groups of yttrium silicates with contrasting Ca and Th contents have been discerned in the Pinciná maar. The first group is typical of high Th + U (13–20 wt.% oxide) and low CaO (0.5–2 wt.%) contents. Analytical totals close to 100% indicate a non-metamict structure without molecular water or hydroxyl groups (Table S11). The crystal formula calculated on the basis of seven oxygen atoms, $(Y_{0.97-1.13}REE_{0.34-0.40}(Fe,Ca,Mn,Mg)_{0.22-0.34}(Th,U)_{0.23-0.32}(Si,Ti)_{1.98-2}O_7$, corresponds to yttrialite-(Y). The mineral is characterized by the dominant coupled substitution $M^{2+} + (U,Th)^{4+} \leftrightarrow (Y,REE)^{3+}$. The chemical analyses are almost ideally aligned along the tie-line connecting the pure yttrialite $(Y,REE)_2Si_2O_7$ and a hypothetical $M^{2+}(U,Th)Si_2O_7$ endmember, the latter reaching 15–35 mol.% in the investigated mineral (Figure 7). The high-Th yttrium silicates from Pinciná are similar to those identified in zircon megacryst from the Fil’akovo maar [1], which are also displayed in Figure 7 for comparison.

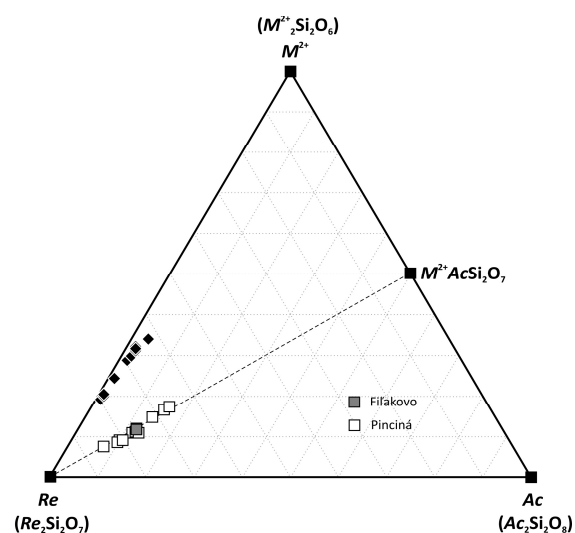


Figure 7. Molecular proportions in high- and low-Th yttrium silicates (open squares and black diamonds, respectively) recalculated from formulae based on seven oxygen atoms. *Re* and *Ac* refer to Y + REE and Th + U, respectively. M^{2+} are large divalent cations (Fe, Ca, Mn, Mg). Data from Fil’akovo maar (shaded squares) are from [1].

The second group of yttrium silicates is characterized by lower ThO_2 (1.2–3.8 wt.%), medium-to-high CaO concentrations (2.9–4.9 wt.% in syenite PI-12, 9.2–10.9 wt.% in syenite HP-3), and elevated amounts of halogens (0.5–1.3 wt.%) (Table S12). Molecular proportions recalculated using seven oxygen atoms yield excessive cations (>4), and a different slope of the exchange vector in the $M^{2+}-(\text{U,Th})^{4+}-(\text{Y,REE})^{3+}$ correlation diagram (Figure 7) compared to the first group. Atomic proportions based on eight cations plotted in the $M^{2+} + (\text{U,Th})^{4+}$ versus $(\text{Y,REE})^{3+}$ coordinates show almost ideal correlation ($r^2 = 0.98$) indicating the heterovalent substitution $Re^{3+} = 4 - 0.5(M^{2+} + Ac^{4+})$ (Figure 8) contrasting with the exchange vector of $Re^{3+} = 2 - (M^{2+} + Ac^{4+})$ in the Th-rich yttrialite. The observed trend reflects the probable solid solution of two yttrialite molecules and one “britholite-Y” molecule (i.e., $2\text{Y}_2\text{Si}_2\text{O}_7 \leftrightarrow \text{Y}_3\text{CaTh}(\text{SiO}_4)_3(\text{OH})_3$). The 77.3–86.7 mol.% of the yttrialite component defines the yttrialite-Y in the syenite PI-12, contrasting with 50.4–60.6 mol.% of the britholite-Y component in the syenite HP-3. The yttrium silicate from zircon xenocryst extracted from tuff (sample P-4) also corresponds to britholite-Y, with 68.1 mol.% of the britholite-Y component.

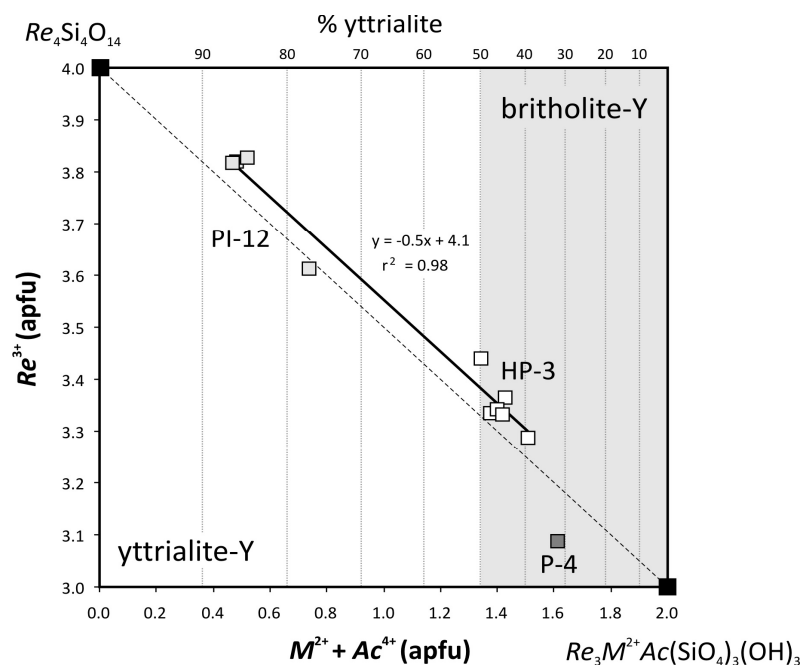


Figure 8. Substitutions in low-Th yttrium silicates from Pinciná maar inferred from atomic proportions recalculated using eight cations. Re and Ac refer to $\text{Y} + \text{REE}$ and $\text{Th} + \text{U}$, respectively. M^{2+} designates large divalent cations (Fe , Ca , Mn , Mg).

4.2.3. Britholite-Ce

Representative analyses of silicates dominated by light rare earth elements associated with chevkinite-Ce are listed in Table S13. Atomic proportions recalculated from formulae based on eight cations plot along the britholite-apatite exchange vector $(\text{Ca} + \text{P}) = \sim 7.86 - (\text{Re} + \text{Si})$ [29]. The $Re + \text{Si}$ values between 6.40 and 6.64 indicate 82–85.1 mol.% britholite-Ce component in the Ca-Ce-silicate from syenite HP-3 (Figure 9a).

The La-Nd silicates in the syenite PI-12 contain more ThO_2 (1.1–7.3 wt.%) and have variable P_2O_5 (6.6–26.8 wt.%), SiO_2 (1.5–20 wt.%), and CaO (7.3–13.2 wt.%) contents compared to the syenite HP-3. $Re + \text{Si}$ values between 2.9 and 5.8 correspond to 37.5–74.6 mol.% britholite-Ce. The perfect $2\text{Ca} = \text{Th} + \text{U}$ substitution contrasting with unsystematic Ca versus P ratios and the position of projection points between the huttonite–monazite and yttrialite–britholite-Y exchange vectors in the $(M^{2+} + \text{Ac})$ versus Re diagram (Figure 9b) indicate a rather complex interplay of monazite, huttonite, britholite-Ce, and apatite molecules. The intersection of yttrialite–britholite-Y and the britholite-Ce–apatite exchange vectors (Figure 9a) indicative of the involvement of the yttrialite molecule in the complex REE-

silicate-phosphate are also noteworthy. A more precise analysis of the mixing trends is precluded by the insufficient number of analyses caused by the mineral scarcity and small dimensions of mineral grains, making the EPMA analyses tricky, as the position of electron beam changes with switching between two different sample currents.

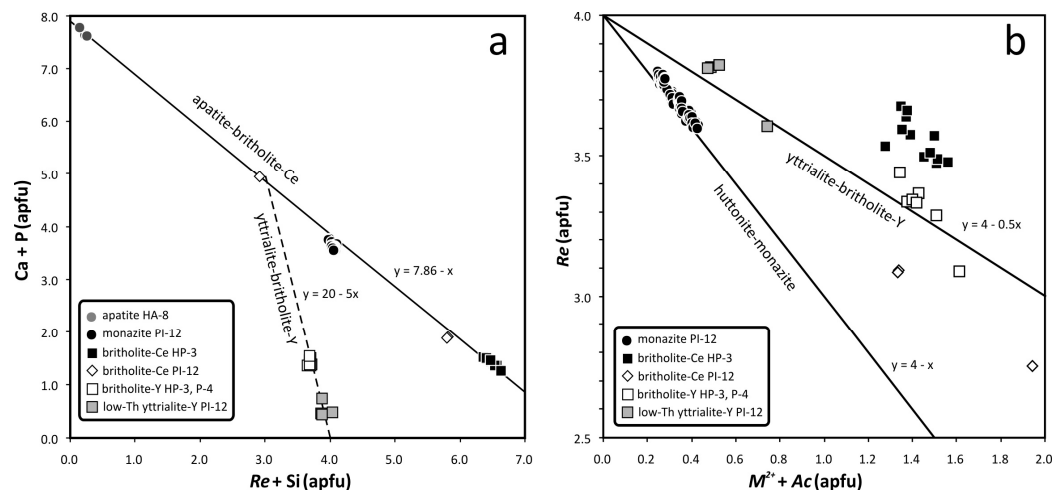


Figure 9. Substitutions in britholite, yttrilite, and monazite from Pinciná maar, and apatite from Hajnáčka diatreme, inferred from atomic proportions recalculated using eight cations. *Re* and *Ac* refer to Y + REE and Th + U, respectively. M^{2+} are large divalent cations (Fe, Ca, Mn, Mg). (a) *Re* + Si versus *Ca* + *P* correlation. (b) M^{2+} + *Ac* versus *Re* correlation, showing the arrangement of monazites from Pinciná maar along the monazite-huttonite tie-line.

4.2.4. Ca-Ce Phosphate

Representative analyses of hydrous Ca-Ce phosphates associated with britholite-Ce and chevkinite-Ce are listed in Table S14. A crystalchemical formula based on four oxygen atoms returned approximately two cations, thus resembling a rhabdophane-like phase. However, low analytical totals (81–88 wt.%) in the analyzed phosphates indicate 2–3 water molecules compared to ideal rhabdophane $CePO_4 \cdot H_2O$ with 7.12 wt.% H_2O . The high CaO contents (5.3–7.2 wt.%, 0.23–0.37 apfu) are also unusual, possibly indicating a greylite component $(Ca,Ce,Th)PO_4 \cdot H_2O$. However, the charge of divalent cations is not counterbalanced by a sufficient amount of large tetravalent cations (Th and U). In addition, up to 1 wt.% halogens may be associated with structurally bound OH. Hence, identification of the hydrous Ca-Ce phosphate remains only provisional, demanding support from additional spectroscopic methods.

4.2.5. Zirconolite

The zirconolites from Hajnáčka diatreme (Table S15) are characterized by high Y + REE contents, 0.20–0.41 apfu, accommodated in the eight-fold-coordinated *A*-site by the incorporation of charge-balancing divalent (mostly Fe^{2+}) and pentavalent (Nb + Ta) cations in the five- or six-fold-coordinated *C*-site. Up to 0.13 apfu of actinides in the *A*-site are accommodated by substituting charge-balancing ferrous iron together with Ti^{4+} in the *C*-site.

The chemical substitutions in zirconolites are characterized by the following exchange vectors, reflecting heterovalent substitutions in several sites (Figure 10):

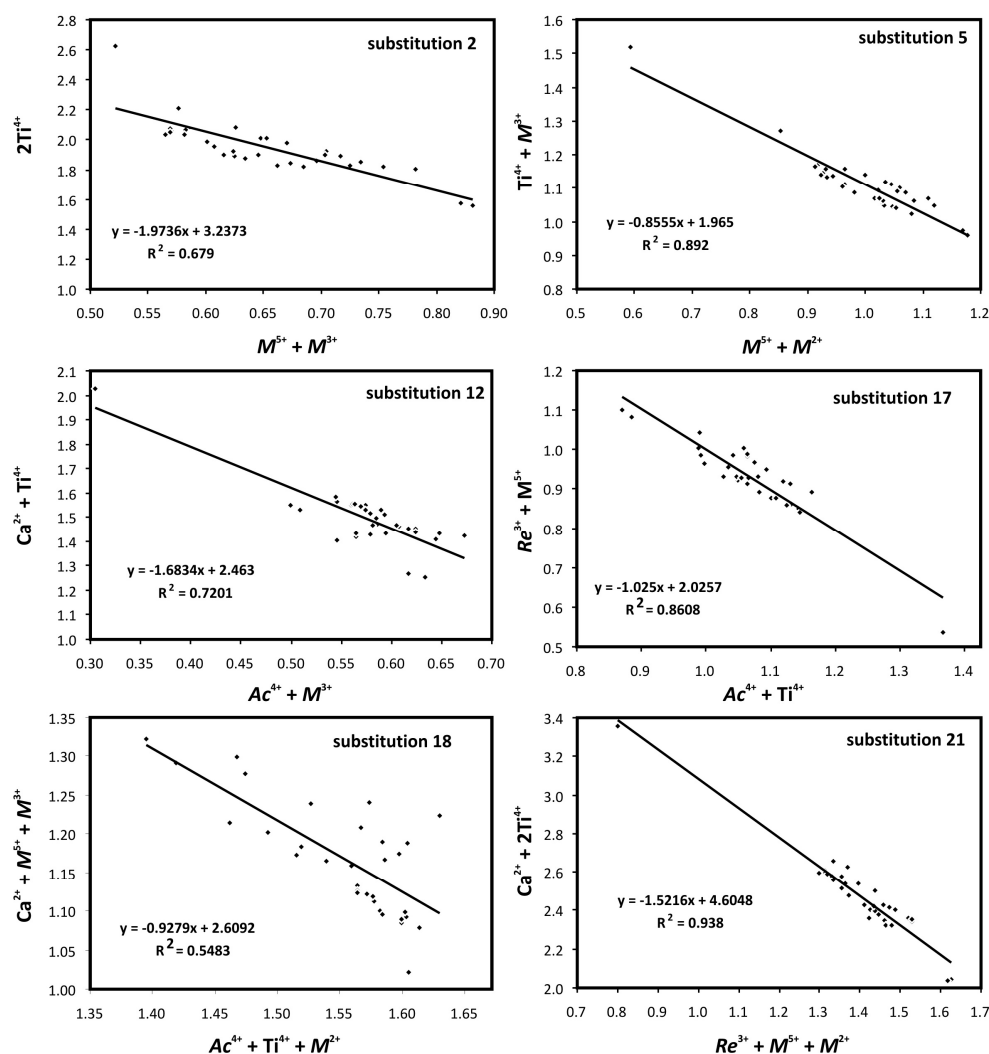


Figure 10. Important substitutions in zirconolites from Hajnáčka. Substitution numbers refer to exchange vectors defined in [27] and Figure 11a,b.

1. $Re^{3+} + M^{5+} + M^{2+} \leftrightarrow Ca^{2+} + 2Ti^{4+}$ ($r^2 = 0.938$),
2. $Re^{3+} + M^{5+} \leftrightarrow Zr^{4+} + Ti^{4+}$ ($r^2 = 0.9325$),
3. $Re^{3+} + 2Ti^{4+} \leftrightarrow Zr^{4+} + M^{5+} + M^{2+}$ ($r^2 = 0.8387$),
4. $M^{5+} + M^{2+} \leftrightarrow Ti^{4+} + M^{3+}$ ($r^2 = 0.892$),
5. $Ac^{4+} + Ti^{4+} \leftrightarrow Re^{3+} + M^{5+}$ ($r^2 = 0.8608$),
6. $Ac^{4+} + M^{2+} \leftrightarrow Ca^{2+} + Ti^{4+}$ ($r^2 = 0.720$),
7. $M^{5+} + M^{3+} \leftrightarrow 2Ti^{4+}$ ($r^2 = 0.679$),
8. $Ac^{4+} + Ti^{4+} + M^{2+} \leftrightarrow Ca^{2+} + M^{5+} + M^{3+}$ ($r^2 = 0.5483$).

The exchange vectors define the compositional space bound by $AcZrTiM^{2+}O_7$, $CaZrTi_2O_7$, $ReZrM^{5+}M^{2+}O_7$, and $CaZrM^{5+}M^{3+}O_7$ endmembers [30].

The Fe^{3+}/Fe_{tot} ratios recalculated from stoichiometry based on four cations and the cationic charge equal to 14 [31] range between 0.10 and 0.45, showing the prevalence of ferrous over ferric iron, and the general prevalence of other than $Ca + Sr M^{2+}$ cations over M^{3+} cations (Al, Bi, Fe^{3+}). Owing to the prevalence of M^{2+} over M^{3+} and the high correlation coefficients of corresponding exchange vectors ($r^2 = 0.72$ – 0.94), the Hajnáčka zirconolites can be classified using triangle (b) in Figure 11.

The following end-members ordered by the decreasing abundance occur in Hajnáčka zirconolites: 1. (Y,REE)Zr(Nb,Ta)(Fe,Mg,Mn)O₇, 2. (Ca,Sr)ZrTi₂O₇, 3. (Ca,Sr)Zr(Nb,Ta)(Fe³⁺,Al,Bi)O₇, 4. (U,Th)ZrTi(Fe,Mg,Mn)O₇, and 5. (Ca,Sr)Ti₃O₇. The first four components are typical of natural zirconolites. The CaTi₃O₇ component known only as synthetic zirconolite [30] attains up to 16.6 mol.%, and is locally the third most abundant component. Proportions of other theoretical endmembers are below 2.7 mol.%.

The zirconolite compositions from Hajnáčka diatreme project within the triangle area bounded by REE-rich members of the zirconolite group—that is, stefanweissite, laachite, and nöggerathite (Figure 11c). One outlier falls outside the field, close to the Ca-apex diagnostic of the common REE-depleted zirconolite CaZrTi₂O₇. Other Hajnáčka zirconolites differ from the holotypes described from the Tertiary Laacher See volcano by lower Mn, Nb, and Ce, and higher Th + U contents (except for laachite). The contents of dominant cations are similar to nöggerathite, despite the proportions of eight-fold-coordinated cations, except Ti, project between stefanweissite and laachite.

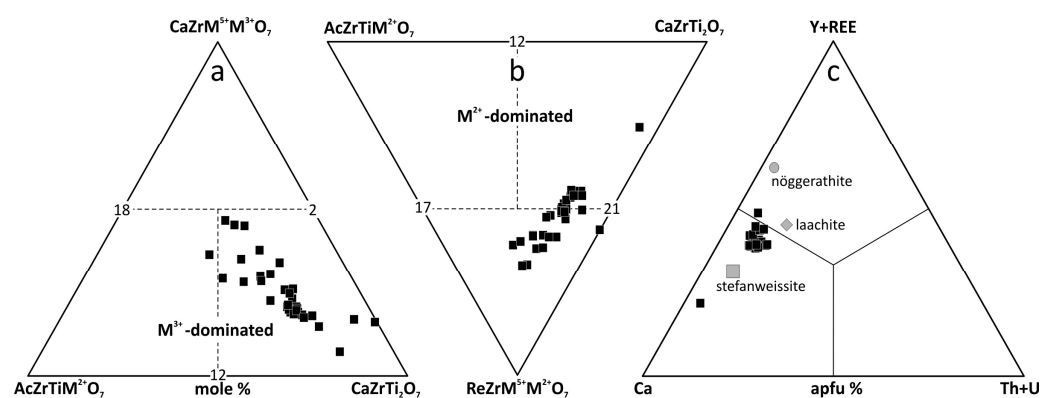


Figure 11. Classification diagrams for M³⁺-dominated (a) and M²⁺-dominated zirconolites (b) based on endmember proportions (mol.%) calculated from crystal formulae based on four cations and a cationic charge equal to 14, with projection points of zirconolites from Hajnáčka (black squares). Numbers on tie-lines refer to the substitutions documented in Figure 10. Boundaries are constructed using the dominant valency rule [32]. (c) Classification diagram based on atomic proportions of eightfold-coordinated cations, with projection points of zirconolites from Hajnáčka (black squares), stefanweissite, laachite, and nöggerathite holotypes from the Tertiary Laacher See volcano of the Eifel region, Germany [33–35]. Boundaries are constructed using the dominant component rule [32].

4.3. Chemical Composition of Silicate Glass

Zircon-hosted glass inclusions large enough to be analyzed by the defocused electron beam yielded a peraluminous alkalic trachyte composition, similar to that of interstitial glass (Figure 12, Table S5). The silicate glass associated with yttrialite and britholite-Y was a metaluminous alkali-calcic trachyte. The interstitial glass associated with zirconolite corresponded to strongly alkalic metaluminous trachyte.

In summary, silicate glasses from Pinciná and Hajnáčka are dominantly potassic and ferroan trachytes with variable alkalinity and aluminosity. Rather peculiar are the presence of quartz in the strongly alkaline syenite xenolith from Hajnáčka and the absence of quartz in the quartz-normative syenite xenolith from Pinciná. Compositions of silicate melt inclusions indicate trachytic parental melts, which are more alkaline in Hajnáčka compared to Pinciná.

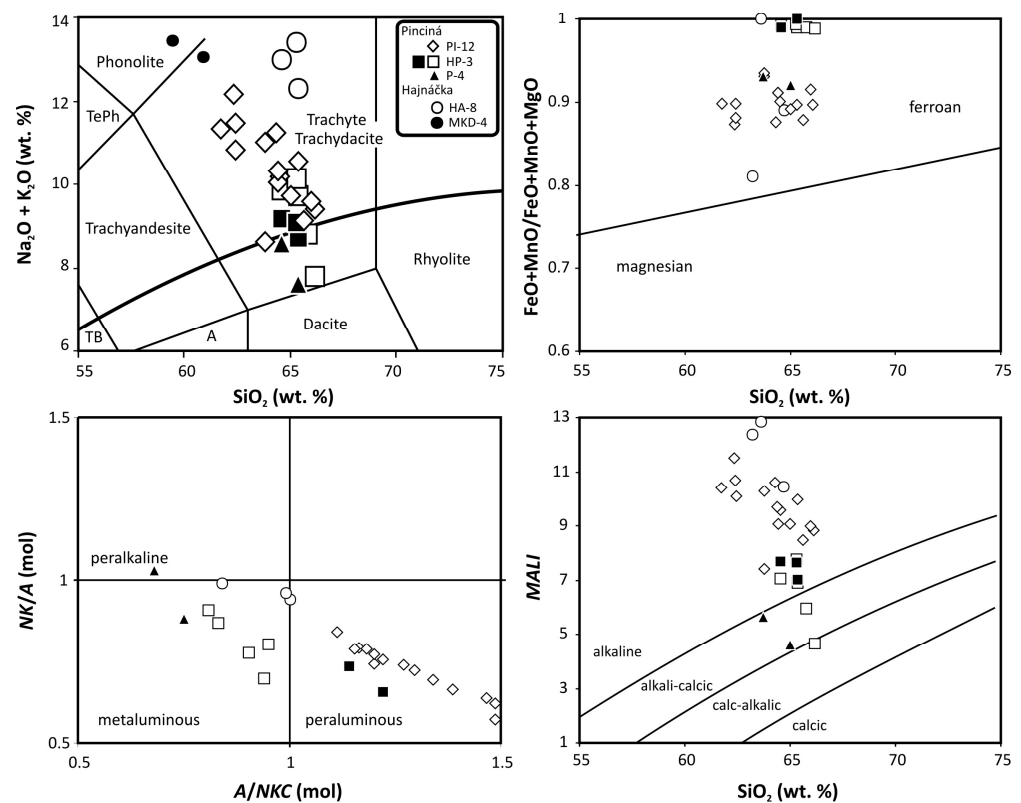


Figure 12. Classification diagrams of magmatic rocks based on major elements [36–38], with projection points of silicate glass from Pinciná (PI, HP, P) and Hajnáčka (HA, MKD) (Table S5). $A/NKC = Al_2O_3 / (CaO + Na_2O + K_2O - 1.67P_2O_5)$, $NK/A = (Na_2O + K_2O) / Al_2O_3$, $MALI = Na_2O + K_2O - CaO$. Black and open symbols refer to silicate glass inclusions in zircons and interstitial glass, respectively. Abbreviations of rock names: TePh—tephriphonolite, TB—trachybasalt, A—andesite.

5. Discussion

5.1. Genetic Constraints from Silicate Glass and Bulk Rock Compositions

Productive syenites enriched in REE-bearing minerals correspond to ferroan, potassic, and locally sodic types, typically representing flotation cumulates from fractionated alkali basalt. Variations in the parental basalt composition resulted in the variable alkalinity of the residual melts, ranging from strongly alkaline-to-peralkaline (HA-8), through medium alkaline (PI-12), to alkali-calcic compositions (HP-3, P-4).

The productive granites enriched in HFSE- and REE-minerals are ferroan and calc-alkalic, whereas barren orthopyroxene granite (pincinite), practically devoid of accessory minerals except for zircon and monazite, is magnesian and calcic [9]. All granite xenoliths are peraluminous.

The melt aluminosity does not correlate well with the alkalinity, which is rather heterogeneous within a single xenolith. For instance, while the interstitial glass in the syenite HP-3 is metaluminous, silicate glass inclusions in zircon and the bulk xenolith composition are both peraluminous. The peraluminous melts are traditionally interpreted as either anatectic crustal melts or those resulting from extensive crustal assimilation of mantle-derived melts. Despite the strong peraluminosity of the productive syenite and granite xenoliths, superchondritic $\epsilon Hf(t)$ values in accessory zircons from both rock types testify to mantle-derived parental magmas unaffected by the crustal assimilation [7].

The increased Ca content in the productive calc-alkalic granite from Čamovce [7,9] with strong peralkaline affinity indicated by AMA could result from the assimilation of crustal limestones. This hypothesis is indirectly supported by the abundant anorthite-Ca-Tschermak clinopyroxene-forsterite-carbonate skarnoid xenoliths in the same lava flow.

Despite the variegated major element compositions, the whole-rock trace element signatures based on Y/Nb, Rb/Nb, and Y/Ce/Nb ratios in the granites and syenites from the northern Pannonian Basin are diagnostic of an A1-type anorogenic igneous assemblage from intra-plate tectonic settings [7,9,18].

5.2. Accessory Mineral Assemblages (AMA)

A total of 20 accessory minerals have been detected in felsic and intermediate igneous xenoliths ejected by Pliocene basalts in the northern Pannonian Basin (Table 1).

Table 1. AMAs identified in syenite and granite xenoliths.

Locality	Pinciná		Hajnáčka	Čamovce
Xenolith	Syenite		Syenite-Carbonatite	Granite
Aluminosity	Peraluminous	Metaluminous	Metaluminous	Peraluminous
Alkalinity	Moderately to Strongly Alkalic	Alkalic to Alkali-Calcic	Strongly Alkalic	Calc-Alkalic
Apatite	+	+	+	+
Baddeleyite			+	
Britholite-Ce	+	+		
Britholite-Y	+	+		
Columbite-Mn				+
Chevkinite-Ce		+		
Fergusonite-Y	+			+
Fersmite/viggezite				+
Ilmenite-Nb			+	+
Monazite-Ce	+			
Pyrochlore				+
Rhabdophane (?)		+		
Rutile-Nb			+	+
Samarskite	+			+
Titanite		+	+	
Uranothorianite	+	?		
Uranothorite	+	?		+
Yttrialite-Y	+	+		
Zircon	+	+	+	+
Zirconolite			+	

Notes: +: present; ?: uncertain; empty space: absent.

Zircon occurs in all xenolith types, though it is preferably concentrated in syenites. Zr/Hf ratios in Pliocene zircon xenocrysts in maar sediments and syenite xenoliths are scattered within an interval between 40 and 90 [1]. The Zr/Hf ratios > 60 reflect a late Zr saturation in alkaline parental melts [39]. Th/U ratios between 0.5 and 8.1 in the xenolith zircons overlap the range of 0.2–4.6 determined in Pliocene xenocrystic zircons [1]. Such high Th/U ratios are also diagnostic of evolved alkaline syenite or phonolite parental melts [40–42] similar to those detected in silicate glass inclusions (Figure 12).

The baddeleyite–titanite–zirconolite assemblage from Hajnáčka diatreme testifies to the reduced silica activity in the parental magma caused by the interaction with the carbonatite melt. Baddeleyite rims around zircon xenocrysts in pyroclastic deposits of a neighboring Hajnáčka-Kostná Dolina maar [43,44] also indicate the interaction with a silica-poor, most probably carbonatitic melt. The high Zr/Hf ratio in the zircon (74–80) is indicative of evolved, alkaline silicate parental melt.

The AMA with chevkinite-Ce and britholite is diagnostic of syenites from Pinciná, which lack the evidence of the silicate magma interaction with carbonates or carbonatites. Britholite-Ce from alkalic syenite has substantially higher ThO₂ content (7.2 wt.%), lower La, Ca, and higher Nd and Sm contents compared to that in less alkalic to alkali-calcic syenite. The excessive P in the alkalic syenite triggered the crystallization of monazite-Ce associated with minerals of the britholite-apatite solid solution series.

Fergusonite-Y occurs in syenite and as well as productive calc-alkalic granite. The syenite-hosted fergusonite is enriched in Ce₂O₃ (up to 4 wt.%) and Nd₂O₃ (up to 5.2 wt.%)

compared with the maxima of 1.5 and 1.8 wt.%, respectively, determined in the fergusonite from granite. Silicate glass inclusions in fergusonite from granite correspond to potassic, ferroan, peraluminous, sub-alkalic granite [7], being thus similar to the bulk rock composition.

Pyrochlore, columbite, subordinate Ca-niobate (fermite/viggeite), Nb-ilmenite, and Nb-rutile also occur in the productive calc-alkalic, peraluminous granite. The AMA is normally diagnostic of peralkaline magmas [45,46]. The relatively Ca-rich granite composition is mirrored in the crystallization of oxycalciopyrochlore and Ca-niobates. The inhibited allanite crystallization is most likely due to the insignificant water dissolved in the parental melt, which precluded the precipitation of OH-bearing minerals besides fluorapatite.

Nb-bearing ilmenite replaced by niobian rutile is typical for strongly alkalic syenite as well as calc-alkalic granite. Significant concentrations of HFSE in Fe,Ti-oxides are regarded as diagnostic of their magmatic origin and close genetic relationship with alkaline rocks and carbonatites [47].

Yttrialite-Y is a diagnostic mineral of syenites from Pinciná maar. Identical yttrialite-Y inclusions in zircon xenocrysts in the Fil'akovo maar [1] unequivocally testify to the syenite reservoir or intrusion beneath both maars.

Compositions of syenite xenoliths accompanying mafic cumulates, granites, and skarns are fairly similar to the xenolithic assemblage found in volcanic ejecta of the dormant Colli Albani volcano in Central Italy [48]. Carbonatite syenites interpreted as solidified crystal-liquid mush have also been described from the Laacher See volcano in the Eifel region, Germany [41,49]; phonolitic volcanoes of the Kula volcanic province of Western Turkey [50]; and Tenerife, Canary Islands [51–53].

5.3. Geochemical Proxies

Additional information regarding the composition of parental magmas can also be obtained from the chemistry of accessory minerals. For instance, zirconolites from Hajnáčka plot within the syenite field and along the syenite-carbonatite boundary in the discrimination diagram correlating HFSE and REE (Figure 13), being thus reliable genetic indicators of alkaline syenite-carbonatite parental magmas.

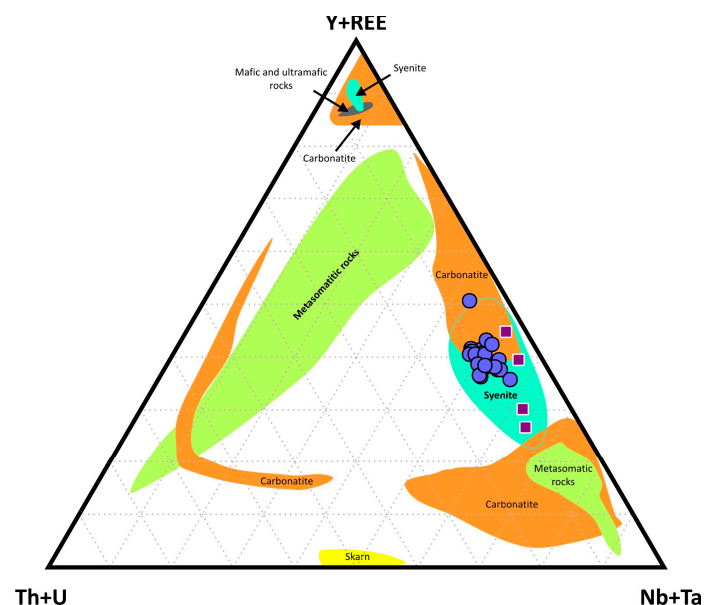


Figure 13. REE–(Th + U)–(Nb + Ta) diagram [28] with projection points of zirconolites from Hajnáčka (blue circles) and compositional fields for zirconolites from metasomatic rocks, skarns, syenites, mafic and ultramafic rocks, and carbonatites compiled from literature. Violet squares are projection points of laachite, stefanweissite, and nöggerathite from an alkaline syenite-carbonatite intrusive complex subjacent to the Laacher See volcano, Eifel volcanic region, Germany [33–35].

Similarly, FeO, $\Sigma\text{YREE}_2\text{O}_3$, and $\text{CaO} + \text{SrO} + \text{MgO} + \text{Al}_2\text{O}_3$ contents in chevkinite-Ce from Pinciná projects along the boundary between Si-undersaturated and Si-oversaturated evolved igneous rocks (Figure 14). The chevkinite-Ce composition from Pinciná is similar to that described from Middle-Miocene alkalic syenite from Ashizuri Peninsula, Japan [54]; Palaeocene granite of St. Kilda Complex, Scotland [55]; alkalic syenite complex of Puttetti, Indonesia [56,57]; Archean peralkaline granite complex of Keivy, Kola Peninsula; and Vishnevye Gory, Ural Mountain Chain of Russia [58].

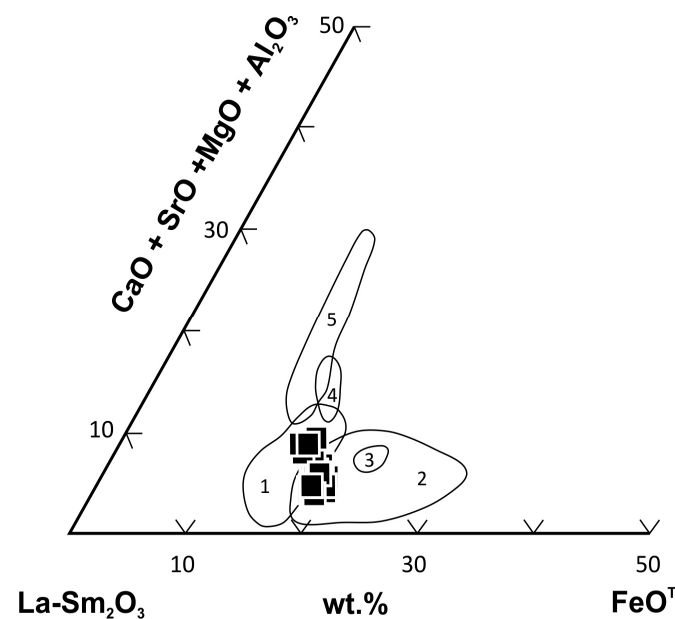


Figure 14. Discrimination diagram [27] correlating chevkinite/perrierite compositions with their host rocks. Black squares are projection points of chevkinite-Ce from Pinciná. 1—Si-oversaturated evolved magmatic rocks, 2—Si-undersaturated evolved magmatic rocks, 3—metasomatic rocks (fenite), 4—granite, 5—mafic and intermediate igneous rocks.

5.4. Ages and Emplacement Depths of Sub-Volcanic Reservoirs

The U-Pb-(Th) ages of zircon and monazite in syenite xenoliths ejected in the Lučenec basin correspond to 5.3–5.9 Ma [1,18], whereas zircons recovered from volcanic structures in Cerová Upland returned U-Pb ages from 6.5 to 1.6 Ma [1,7,20,43]. These dates constrain the lifespan of two separated magmatic reservoirs occurring in both areas. Both reservoirs produced ferroan, potassic, dominantly peraluminous syenites, but the southern, more alkalic reservoir beneath the Hajnáčka diatreme was recharged with carbonatite magma. Skarnoid xenoliths in this area also bear a piece of indirect evidence for crustal limestones interacting with or assimilated in the magmatic reservoir. The southern reservoir possibly extends from the area between Fiľakovo town and the Hajnáčka village northwards (Hodejov maar), eastwards (Gemerské Dechtáre maar), and north-eastwards (Tachty diatreme), covering an area of about 200 km². The areal extent of the northern reservoir in the Lučenec basin is unknown, as the xenolith and xenocryst data are only restricted to the Pinciná maar.

Both magmatic reservoirs occur in highly conductive zones detected by magnetotelluric sounding [59,60]. The conductive zone in the Lučenec basin is traced down to the depth of 15 km and probably more. The conductive zone beneath Fiľakovo maar and Hajnáčka diatreme is underlain in the depth of ~5 km by moderately resistive domain interpreted as a low-conductivity (possibly Cadomian or Proterozoic) crystalline fundament. The high-conductivity zones are recently interpreted as water-saturated Neogene sediments in shallow parts and fluid-saturated pathways with ore accumulations in deeper parts, aligned along regional fault zones.

Stratified magmatic reservoirs beneath intra-plate volcanoes are located in relatively shallow depths, for example, 5–6 km beneath the Laacher See volcano [41], ~12 km beneath

the Tenerife island [53], and ~10 km beneath the Coli Albani maar [48]. The emplacement depth of the reservoir sampled by the Pinciná maar in the Lučenec basin has been estimated from the density of primary CO₂-rich inclusions, and the approximate temperature of 800–900 °C inferred from zircon morphology. The inferred pressures—from 2.5 to 2.8 kbar for oxidized syenites, and 4.3–5.2 kbar for reduced syenites, including PI-12 and HP-3—testify to the magma underplating, stagnation, and differentiation in at least two separated horizons in the depth interval from 10 to 20 km [6]. However, these depth estimates can be biased by the loss of some fluid content from fluid inclusions through decrepitation cracks, and by the lacking independent thermobarometric control from mafic mineral assemblages.

Emplacement depth of the carbonatite-syenite intrusives beneath the Hajnáčka diatreme in the Cerová Upland can only be roughly estimated from the titanite-ilmenite-rutile equilibrium, which has a triple point at ~13 kbar and 780 °C in the tholeiite basalt-H₂O system. The magmatic rutile is stable above 13–14 kbar at temperatures between 700 and 900 °C [61]. The lower pressure titanite-ilmenite assemblage is dominant in Ca-poor systems below 9 kbar at 700 °C, but may be stable at higher pressures in Ca-richer rocks [62].

The ilmenite-rutile transformation (Figure 4b) accompanied by titanite resorption in the interstitial silicate melt (Figure 4a) and especially aragonite crystallization in intergranular carbonate ocelli (Figure 4d) are indicative of crystallization pressures above the titanite-ilmenite stability limit. Assuming the minimum temperature of 700 °C, a pressure of >15 kbar corresponding to depths >45 km would be needed to crystallize the magmatic aragonite and to allow the ilmenite-rutile transformation. The crystallization of primary magmatic aragonite is provisionally explained as a record of advective supra-lithostatic overpressure caused by expanding gas bubbles in a quasi-incompressible silicate melt [24]. If existing, this effect would make reliable pressure determinations from mineral assemblages problematic. The magmatic aragonite has never been detected in igneous xenoliths from the Lučenec basin, although sporadic calcite inclusions in kaersutite and clinopyroxene megacrysts, as well as carbonatite and carbonated pyroxenite xenoliths, do occur in the basaltic lava flow near Mašková village [63], located northwest of Pinciná maar. It seems therefore likely that the aragonite crystallization from syenite and carbonatite in the Cerová Upland has a special, yet poorly understood, causal relationship with the pressure regime of the southern magmatic reservoir. It looks quite reasonable that the overpressures are due to extensive CO₂-devolatilization resulting from the assimilation of limestones or the mingling of alkalic silicate and carbonatite magmas.

The recently active, shallow magmatic reservoirs in the Lučenec basin and the Cerová Upland are unlikely despite the occurrence of relatively young, 1.6 Ma old magmatic zircons recovered from maar sediments [43] and even younger, Early Pleistocene (1.2–1.5 Ma) basalts NE of Filákovo [16]. The modern regional heat flow in this area, ~90 mWm⁻², indicates partially molten masses ~80–90 km deep [64,65].

6. Conclusions

- Pliocene basalts in Carpathian back-arc basin ejected fragments of stratified subvolcanic magmatic reservoirs or intrusive complexes.
- Zircon crystals and fragments in pyroclastic deposits represent relics of disintegrated syenite xenoliths.
- Accessory mineral assemblages (AMA) in xenoliths and pyroclastic deposits reflect several types of parental melts:
 - Zirconolite and baddeleyite indicate carbonatite-alkalic syenite intrusives;
 - Yttrialite, monazite, chevkinite, and britholite are diagnostic of moderately alkalic to alkali-calcic syenite intrusives;
 - Pyrochlore, columbite-Mn and Ca-niobates crystallized from anhydrous calc-alkalic granites with strong peralkaline affinity.
- The stratified subvolcanic reservoir beneath Lučenec basin is emplaced 10–20 km deep.
- The reservoir beneath Cerová Upland, probably ~200 km² in area, is emplaced more than 45 km deep.

- Zirconolite, yttrialite, and britholite-Y are new minerals described in the Western Carpathian realm.

Supplementary Materials: The following data are available online at <https://www.mdpi.com/article/10.3390/min11040369/s1>, Table S1: EPMA analytical conditions, Table S2: Major and trace element analyses of xenoliths, Table S3: EPMA of monazite, Table S4: EPMA of fergusonite, Table S5: EPMA of silicate glass, Table S6: EPMA of ilmenite and rutile, Table S7: EPMA of apatite, Table S8: EPMA of titanite, Table S9: EPMA of zircon and baddeleyite, Table S10: EPMA of chevkinite, Table S11: EPMA of high-Th yttrium silicates, Table S12: EPMA of low-Th yttrium silicates, Table S13: EPMA of britholite, Table S14: EPMA of rhabdophane, Table S15: EPMA of zirconolite.

Author Contributions: Conceptualization, M.H. and V.H.; methodology and software, P.K.; writing—original draft preparation, review, and editing, V.H.; project administration, M.H. All authors have read and agreed to the published version of the manuscript.

Funding: This research was funded by the VEGA grant agency, grant number 1/0143/18.

Data Availability Statement: The data presented in this study are available in this article and the attached Electronic Supplementary Material.

Acknowledgments: The original draft greatly benefited from constructive comments from three anonymous reviewers.

Conflicts of Interest: The authors declare no conflict of interest. The funders had no role in the design of the study; in the collection, analyses, or interpretation of data; in the writing of the manuscript, or in the decision to publish the results.

References

1. Hurai, V.; Danišik, M.; Huraiová, M.; Paquette, J.-L.; Adam, A. Combined U/Pb and (U–Th)/He geochronometry of basalt maars in Western Carpathians: Implications for age of intraplate volcanism and origin of zircon metasomatism. *Contrib. Mineral. Petrol.* **2013**, *166*, 1235–1251. [\[CrossRef\]](#)
2. Nemec, O.; Huraiová, M. Provenance study of detrital garnets and rutiles from basaltic pyroclastic rocks of southern Slovakia (Western Carpathians). *Geol. Carpath.* **2018**, *69*, 17–29. [\[CrossRef\]](#)
3. Huraiová, M.; Konečný, P.; Konečný, V.; Simon, K.; Hurai, V. Mafic and felsic igneous xenoliths in late Tertiary alkaline basalts: Fluid inclusion and mineralogical evidence for a deep-crustal magmatic reservoir in the Western Carpathians. *Eur. J. Mineral.* **1996**, *8*, 901–916. [\[CrossRef\]](#)
4. Konečný, P.; Konečný, V.; Lexa, J.; Huraiová, M. Mantle xenoliths in alkali basalts of southern Slovakia. *Acta Volcanol.* **1995**, *7*, 241–248.
5. Hurai, V.; Simon, K.; Wiechert, U.; Hoefs, J.; Konečný, P.; Huraiová, M.; Pironon, J.; Lipka, J. Immiscible separation of metalliferous Fe/Ti-oxide melts from fractionating alkali basalt: P–T–fO₂ conditions and two-liquid elemental partitioning. *Contrib. Mineral. Petrol.* **1998**, *133*, 12–29. [\[CrossRef\]](#)
6. Huraiová, M.; Dubessy, J.; Konečný, P.; Simon, K.; Král, J.; Zielinski, G.; Lipka, J.; Hurai, V. Glassy orthopyroxene granodiorites of the Pannonian Basin: Tracers of ultra-high-temperature deep-crustal anatexis triggered by Tertiary basaltic volcanism. *Contrib. Mineral. Petrol.* **2005**, *148*, 615–633. [\[CrossRef\]](#)
7. Huraiová, M.; Paquette, J.-L.; Konečný, P.; Gannoun, A.-M.; Hurai, V. Geochemistry, mineralogy, and zircon U–Pb–Hf isotopes in peraluminous A-type granite xenoliths in Pliocene–Pleistocene basalts of northern Pannonian Basin (Slovakia). *Contrib. Mineral. Petrol.* **2017**, *172*, 59. [\[CrossRef\]](#)
8. Huraiová, M.; Konečný, P.; Hurai, V. Niobium mineralogy of Pliocene A1-type granite of the Carpathian back-arc basin, Central Europe. *Minerals* **2019**, *9*, 488. [\[CrossRef\]](#)
9. Huraiová, M.; Hurai, V.; Paquette, J.-L. Petrogenesis of Miocene–Pliocene A-type granitoids of southern Slovakia. *Acta Geol. Slov.* **2015**, *7*, 37–50. (In Slovak with English Resume).
10. Dérerová, J.; Zeyen, H.; Bielik, M.; Salman, K. Application of integrated geophysical modelling for determination of the continental lithospheric thermal structure in the eastern Carpathians. *Tectonics* **2006**, *25*, TC3009. [\[CrossRef\]](#)
11. Tašárová, A.; Afonso, J.C.; Bielik, M.; Götze, H.-J.; Hók, J. The lithospheric structure of the Western Carpathian–Pannonian Basin region based on the CELEBRATION 2000 seismic experiment and gravity modeling. *Tectonophysics* **2009**, *475*, 454–469. [\[CrossRef\]](#)
12. Konečný, V.; Kováč, M.; Lexa, J.; Šefara, J. Neogene evolution of the Carpatho-Pannonian region: An interplay of subduction and back-arc diapiric uprising in the mantle. *EGU Stephan Mueller Spec. Pub. Ser.* **2002**, *1*, 105–123. [\[CrossRef\]](#)
13. Nemcok, M.; Pospíšil, L.; Lexa, J.; Donelick, R.A. Tertiary subduction and slab break-off model of the Carpathian–Pannonian region. *Tectonophysics* **1998**, *295*, 307–340. [\[CrossRef\]](#)

14. Konečný, V.; Balogh, K.; Orlický, O.; Lexa, J.; Vass, D. Evolution of the Neogene-Quaternary alkali basalt volcanism in central and southern Slovakia (West Carpathians). In Proceedings of the XV Carpathian Balkan Geological Association, Athens, Greece, 17–20 September 1995; pp. 533–538.
15. Konečný, V.; Lexa, J.; Balogh, K. Neogene-Quaternary alkali basalt volcanism in Central and Southern Slovakia (Western Carpathians). *Geolines* **1999**, *9*, 67–75.
16. Vass, D.; Elečko, M.; Konečný, V. *Geology of the Lučenská kotlina Depression and Cerová vrchovina Upland*; D. Štúr Publishing House: Bratislava, Slovakia, 2007; pp. 1–284.
17. Vass, D.; Kraus, I. Two basalts of different age in southern Slovakia and their relation to the Poltár Formation. *Miner. Slov.* **1985**, *17*, 435–440. (In Slovak)
18. Hurai, V.; Paquette, J.-L.; Huraiová, M.; Konečný, P. U-Th-Pb geochronology of zircon and monazite from syenite and pincinite xenoliths in Pliocene alkali basalts of intra-Carpathian back-arc basin. *J. Volcanol. Geotherm. Res.* **2010**, *198*, 275–287. [[CrossRef](#)]
19. Pécskay, Z.; Lexa, J.; Szakács, A.; Seghedi, I.; Balogh, K.; Konečný, V.; Zelenka, T.; Kovacs, M.; Póka, T.; Fülöp, A.; et al. Geochronology of Neogene-Quaternary magmatism in the Carpathian arc and intra-Carpathian area. *Geol. Carpath.* **2006**, *57*, 511–530.
20. Paquette, J.-L.; Huraiová, M.; Nemeč, O.; Gannoun, A.-M.; Šarinová, K.; Hurai, V. Origin and provenience of 2 Ma–2 Ga zircons ejected by phreatomagmatic eruptions of Pliocene basalts in southern Slovakia. *Int. J. Earth Sci.* **2019**, *108*, 2607–2623. [[CrossRef](#)]
21. Merlet, C. An accurate computer correction program for quantitative electron probe microanalysis. *Microchim. Acta* **1994**, *114*, 363–376. [[CrossRef](#)]
22. Āmli, R.; Griffin, W.L. Standards and correction factors for microprobe analysis of REE minerals. *Am. Mineral.* **1975**, *60*, 599–606.
23. Konečný, P.; Siman, P.; Holický, I.; Janák, M.; Kollárová, V. Method of monazite dating by means of the microprobe. *Miner. Slov.* **2004**, *36*, 225–235. (In Slovak)
24. Hurai, V.; Huraiová, M.; Milovský, R.; Luptáková, J.; Konečný, P. High-pressure aragonite phenocrysts in carbonatite and carbonated syenite xenoliths within an alkali basalt. *Am. Mineral.* **2013**, *98*, 1074–1077. [[CrossRef](#)]
25. Huraiová, M.; Konečný, P.; Hurai, V. Chevkinite-Ce-REE-Ti silicate from syenite xenoliths in the Pinciná basaltic maar near Lučenec (Southern Slovakia). *Miner. Slov.* **2007**, *39*, 255–268. (In Slovak)
26. Malcherek, T.; Schlüter, J.; Schäfer, C. Perrietite-(Ce) from the Laacher See tephra, Eifel, Gemrany, and the modular character of the chevkinite group of minerals. *Phys. Chem. Mineral.* **2021**, *48*, 10. [[CrossRef](#)]
27. Macdonald, R.; Belkin, H.E. Compositional variations in minerals of the chevkinite group. *Mineral. Mag.* **2002**, *66*, 1075–1098. [[CrossRef](#)]
28. Vlach, S.R.F.; Gualda, G.A.R. Allanite and chevkinite in A-type granites and syenites of the Graciosa Province, southern Brazil. *Lithos* **2007**, *97*, 98–121. [[CrossRef](#)]
29. Zozulya, D.; Lyalina, L.; Macdonald, R.; Bagiński, B.; Savchenko, Y.; Jokubauskas, P. Britholite group minerals from REE-rich lithologies of Keivy alkali granite-nepheline syenite complex, Kola Peninsula, NW Russia. *Minerals* **2019**, *9*, 732. [[CrossRef](#)]
30. Gieré, R.; Williams, C.T.; Lumpkin, G.R. Chemical characteristics of natural zirconolite. *Schweiz. Miner. Petrogr.* **1998**, *78*, 433–459.
31. Hurai, V.; Huraiová, M.; Gajdošová, M.; Konečný, P.; Slobodník, M.; Siegfried, P.R. Compositional variations of zirconolite from the Evate apatite deposit (Mozambique) as an indicator of magmatic-hydrothermal conditions during post-orogenic collapse of Gondwana. *Mineral. Petrol.* **2018**, *112*, 279–296. [[CrossRef](#)]
32. Hattert, F.; Burke, E.A.J. The IMA-CNMNC dominant-constituent rule revisited and extended. *Can. Mineral.* **2008**, *46*, 717–728. [[CrossRef](#)]
33. Chukanov, N.V.; Krivovichev, S.V.; Pakhomova, A.S.; Pekov, I.V.; Schäfer, C.; Viggasina, M.F.; Van, K.V. Laachite, $(Ca,Mn)_2Zr_2Nb_2TiFeO_{14}$, a new zirconolite-related mineral from the Eifel volcanic region, Germany. *Eur. J. Mineral.* **2014**, *26*, 103–111. [[CrossRef](#)]
34. Chukanov, N.V.; Zubkova, N.V.; Britvin, S.N.; Pekov, I.V.; Viggasina, M.F.; Schäfer, C.; Ternes, B.; Schüller, W.; Polekhovskiy, Y.S.; Ermolaeva, V.N.; et al. Nöggerathite-(Ce),(Ce,Ca) $_2Zr_2(Nb,Ti)(Ti,Nb)_2Fe^{2+}O_{14}$, a new zirconolite-related mineral from the Eifel volcanic region, Germany. *Minerals* **2018**, *8*, 449. [[CrossRef](#)]
35. Chukanov, N.V.; Zubkova, N.V.; Pekov, I.V.; Viggasina, M.F.; Polekhovskiy, Y.S.; Ternes, B.; Schüller, W.; Britvin, S.N.; Pushcharovskiy, D.Y. Stefanweissite, $(Ca,REE)_2Zr_2(Nb,Ti)(Ti,Nb)_2Fe^{2+}O_{14}$, a new zirconolite-related mineral from the Eifel paleovolcanic region, Germany. *Mineral. Mag.* **2019**, *83*, 607–614. [[CrossRef](#)]
36. Le Maitre, R.W.; Streckeisen, A.; Zanettin, B.; Le Bas, M.J.; Bonin, B.; Bateman, P.; Bellieni, G.; Dudek, A.; Efremova, S.; Keller, J.; et al. *Igneous Rocks: A Classification and Glossary of Terms*, 2nd ed.; Cambridge University Press: Cambridge, UK, 2002; pp. 1–236.
37. Frost, B.R.; Frost, C.D. A geochemical classification for feldspathic igneous rocks. *J. Petrol.* **2008**, *49*, 1955–1969. [[CrossRef](#)]
38. Frost, C.D.; Frost, B.R. On ferroan (A-type) granitoids: Their compositional variability and modes of origin. *J. Petrol.* **2011**, *52*, 39–53. [[CrossRef](#)]
39. Boehnke, P.; Watson, E.B.; Trail, D.; Harrison, T.M.; Schmitt, A.K. Zircon saturation re-visited. *Chem. Geol.* **2013**, *351*, 324–334. [[CrossRef](#)]
40. Belousova, E.A.; Griffin, W.L.; O'Reilly, S.Y.; Fisher, N.I. Igneous zircon: Trace element composition as an indicator of source rock type. *Contrib. Mineral. Petrol.* **2002**, *143*, 602–622. [[CrossRef](#)]
41. Schmitt, A.K.; Wetzell, F.; Cooper, K.M.; Zou, H.; Wörner, G. Magmatic longevity of Laacher See Volcano (Eifel, Germany) indicated by U-Th dating of intrusive carbonatites. *J. Petrol.* **2010**, *51*, 1053–1085. [[CrossRef](#)]

42. Schmitt, A.K.; Klitzke, M.; Gerdes, A.; Schäfer, C. Zircon hafnium-oxygen isotope and trace element petrochronology of intraplate volcanic rocks from the Eifel (Germany) and implications for mantle versus crustal origins of zircon megacrysts. *J. Petrol.* **2017**, *58*, 1841–1870. [[CrossRef](#)]
43. Hurai, V.; Paquette, J.-L.; Huraiová, M.; Sabol, M. U-Pb geochronology of zircons from fossiliferous sediments of the Hajnáčka I maar (Slovakia)—Type locality of the MN 16a biostratigraphic subzone. *Geol. Mag.* **2012**, *149*, 989–1000. [[CrossRef](#)]
44. Huraiová, M.; Hurai, V.; Konečný, P. Finding of baddeleyite (ZrO₂) in basaltic maar near Hajnáčka (southern Slovakia). *Miner. Slov.* **2011**, *43*, 255–262. (In Slovak)
45. Hirtopanu, P.; Fairhurst, R.J.; Jakab, G. Niobian rutile and its associations at Jolotca, Ditrau alkaline intrusive massif, east Carpathians, Romania. *Proc. Rom. Acad. Ser. B* **2015**, *17*, 39–55.
46. Gronen, L.H.; Sindern, S.; Katzmarzyk, J.L.; Bormann, U.; Hellman, A.; Wotruba, H.; Meyer, F.M. Mineralogical and chemical characterization of Zr-REE-Nb ores from Khalzan Buregtei (Mongolia)—Approaches to more efficient extraction of rare metals from alkaline granitoids. *Minerals* **2019**, *9*, 217. [[CrossRef](#)]
47. Meinhold, G. Rutile and its applications in earth sciences. *Earth Sci. Rev.* **2010**, *102*, 1–28. [[CrossRef](#)]
48. Di Rocco, T.; Freda, C.; Gaeta, M.; Mollo, S.; Dallai, L. Magma chambers emplaced in carbonate substrate: Petrogenesis of skarn and cumulate rocks and implications for CO₂ degassing in volcanic areas. *J. Petrol.* **2012**, *53*, 2307–2332. [[CrossRef](#)]
49. Tait, S.R.; Wörner, G.; Bogaard, P.V.D.; Schmincke, H.-U. Cumulate nodules as evidence for convective fractionation in a phonolite magma chamber. *J. Volcanol. Geotherm. Res.* **1989**, *37*, 21–37. [[CrossRef](#)]
50. Holness, M.B.; Bunbury, J.M. Insights into continental rift-related magma chambers: Cognate nodules from the Kula Volcanic Province, Western Turkey. *J. Volcanol. Geotherm. Res.* **2006**, *153*, 241–261. [[CrossRef](#)]
51. Wolff, J.A. Crystallization of nepheline syenite in a subvolcanic magma system: Tenerife, Canary Islands. *Lithos* **1987**, *20*, 207–223. [[CrossRef](#)]
52. Stock, M.J.; Taylor, R.N.; Gernon, T.M. Triggering of major eruptions recorded by actively forming cumulates. *Sci. Rec.* **2012**, *2*, 731. [[CrossRef](#)]
53. Sliwinski, J.T.; Bachmann, O.; Ellis, B.S.; Dávila-Harris, P.; Nelson, B.K.; Dufek, J. Eruption of shallow crystal cumulates during explosive phonolitic eruptions on Tenerife, Canary Islands. *J. Petrol.* **2015**, *56*, 2173–2194. [[CrossRef](#)]
54. Imaoka, T.; Nakashima, K. Chevkinite in syenites from Cape Ashizuri. Shikoku Island, Japan. *Neu. Jb. Mineral. Abh. Mh.* **1994**, *8*, 358–366.
55. Harding, R.R.; Merriman, R.J.; Nancarrow, P.H.A. A note on the occurrence of chevkinite, allanite and zirkelite on St Kilda, Scotland. *Miner. Mag.* **1982**, *46*, 445–448. [[CrossRef](#)]
56. Miyazaki, T.; Santosh, M. Cooling history of the Puttetti alkali syenite pluton, southern India. *Gondwana Res.* **2005**, *8*, 567–574. [[CrossRef](#)]
57. Semenov, E.I.; Santosh, M. Rare metal mineralization in alkaline pegmatites of southern Indian granulite terrain. *Gondwana Res.* **1997**, *1*, 152–153. [[CrossRef](#)]
58. Macdonald, R.; Bagiński, B.; Kartashov, P.; Zozulya, D.; Dzierżanowski, P. Chevkinite-group minerals from Russia and Mongolia: New compositional data from metasomatites and ore deposits. *Mineral. Mag.* **2012**, *76*, 535–549. [[CrossRef](#)]
59. Bezák, V.; Pek, J.; Majcin, D.; Bučová, J.; Šoltis, T.; Bilčík, D.; Klanica, R. Geological interpretation of magnetotelluric sounding in the southern part of seismic profile 2T (Central Slovakia). *Contrib. Geophys. Geod.* **2015**, *45*, 1–11. [[CrossRef](#)]
60. Bezák, V.; Pek, J.; Vozár, J.; Majcin, D.; Bielik, M.; Tomek, Č. Geoelectrically distinct zones in the crust of the Western Carpathians: A consequence of Neogene strike-slip tectonics. *Geol. Carpath.* **2020**, *71*, 14–23. [[CrossRef](#)]
61. Liou, J.G.; Zhang, R.; Ernst, W.G.; Liu, J.; McLimans, R. Mineral paragenesis in the Piampaludo eclogitic body, Gruppo di Voltri, Western Ligurian Alps. *Schweiz. Miner. Petrogr. Mitt.* **1998**, *78*, 317–335.
62. Angiboust, S.; Harlov, D. Ilmenite breakdown and rutile-titanite stability in metagranitoids: Natural observations and experimental results. *Am. Mineral.* **2017**, *102*, 1696–1708. [[CrossRef](#)]
63. Hurai, V.; Huraiová, M.; Konečný, P.; Thomas, R. Mineral-melt-fluid composition of carbonate-bearing cumulate xenoliths in Tertiary alkali basalts of southern Slovakia. *Miner. Mag.* **2007**, *71*, 63–79. [[CrossRef](#)]
64. Majcin, D.; Dudášová, V.; Tsvyashchenko, A.A. Tectonics and temperature field along the carpathian profile 2T. *Contrib. Geophys. Geod.* **1998**, *28*, 104–114.
65. Majcin, D.; Král, M.; Bilčík, D.; Šujan, M.; Vranovská, A. Thermal conditions for HDR resources in the region of Slovakia. *Contrib. Geophys. Geod.* **2017**, *47*, 1–22. [[CrossRef](#)]